

# Enhanced mechanical properties and corrosion resistance by minor Gd alloying with a hot-extruded Mg alloy

Huai Yao<sup>a,b</sup>, Yi Xiong<sup>a</sup>, Xinying Shi<sup>c</sup>, Harishchandra Singh<sup>d</sup>, Marko Huttula<sup>d,a</sup>, Shubo Wang<sup>d</sup>, Wei Cao<sup>d</sup>

<sup>a</sup>*School of Materials Science and Engineering, Henan University of Science and Technology, Luoyang Henan 471023, China*

<sup>b</sup>*Collaborative Innovation Center of Nonferrous Metals of Henan Province, Luoyang Henan 471023, China*

<sup>c</sup>*School of Physics and Electronic Engineering, Jiangsu Normal University, Xuzhou Jiangsu, 221116, China*

<sup>d</sup>*Nano and Molecular Systems Research Unit, University of Oulu, FI-90014, Finland*

**ABSTRACT:** The microstructure, mechanical properties, and degradation behavior of as-extruded Mg-1.8Zn-0.5Zr-xGd alloys (x=0, 0.5, 1.0, 1.5, 2.0, 2.5 wt%) are investigated. During extrusion, dynamic recrystallization occurs in the alloy and the grain size gradually decreases with increasing Gd content. The mechanical properties and corrosion resistance of the alloys are significantly enhanced by Gd alloying. When the Gd content is 1.5wt%, nanoscale particles of (Mg, Zn)<sub>3</sub>Gd and Mg<sub>2</sub>Zn<sub>11</sub> phases that have a coherent interface with the matrix begin to precipitate out. Under the combined effect of solid solution strengthening, fine grain strengthening and precipitation strengthening, the alloys with 1.5-2.0wt% Gd have a combination of excellent mechanical properties and corrosion resistance. A three-stage corrosion mechanism, including sequential stages from hydroxidation, phosphatization and hydroxidation, to formation-dissolution dynamic equilibrium, is proposed through electrochemical measurements and corroded surface analyses. This extruded Mg-1.8Zn-0.5Zr-(1.5-2.0)Gd alloys can be regarded as the potential candidate for using as biodegradable magnesium implants.

**Keywords:** Magnesium alloys; Microstructure; Mechanical properties; Corrosion; Biodegradation.

## 1. Introduction

Magnesium (Mg) alloys have attracted considerable attentions as biodegradable

implant materials due to their outstanding biocompatibility and biodegradation together with efficient mechanical properties [1-2]. However, some drawbacks, including rapid corrosion rate due to localized corrosion and relatively low strength compared with stainless steels and Ti alloys, have limited their extensive clinical applications [3].

In order to improve the mechanical properties and corrosion resistance of Mg alloys, alloying and microstructure manipulation are feasible approaches. Zn and Zr have been selected as they are nutrient elements to the human body [4]. A small amount of Zn (~2.0wt%) is believed to form a protective film on the surface of the Mg alloy, which improves its corrosion resistance [5]. Alloying with Zr, a useful grain refinement element, can also improve the mechanical properties and corrosion resistance of Mg alloy [6]. Recent researches have found that the addition of RE (rare earth) elements in Mg-Zn-Zr based alloys enhance the mechanical properties and corrosion resistance [7-9]. Meanwhile, thermal mechanical deformations, such as hot extrusion and rolling, are also used to achieve enhanced mechanical properties in these alloys [10-12]. For example, high ultimate tensile strength (UTS) of 285 MPa, yield strength (YS) of 200 MPa and elongation to failure (EL) of 23% were achieved in Mg-1Zn-0.4Zr-8Gd alloy after hot extrusion compared with the as-cast one [13]. Hot extrusion of as-cast Mg-0.22Zn-0.44Zr-3.09Nd alloy led to an increase in UTS to 307 MPa, YS to 293 MPa and EL to 15.9% [14]. Additionally, the as-cast Mg-2.0Zn-0.5Zr-3.0Gd alloy exhibited a corrosion rate of less than 0.5 mm/y after hot extrusion [15]. Nevertheless, the inhomogeneous distribution of secondary phases due to the addition of alloying elements in as-extruded Mg alloy can lead to severe localized corrosion [16]. Wang et al. reported that a homogenization treatment of Mg-Zn-Zr-Y alloy could help to overcome this shortcoming [17]. A Mg-2.4Zn-0.8Gd alloy with a prior solid solution treatment before extrusion showed an improved corrosion resistance compared with the one without solution treatment. Such improvements were further ascribed to the more uniform grain structure and dispersed secondary phases [18]. Despite the improvements in mechanical properties and corrosion resistance, most of the aforementioned RE elements are hepatotoxic and

hazardous to a person's health. Recent studies on Gd containing Mg alloys show that the Gd released by the alloy during degradation is harmless to the human body and has a certain anti-cancer effect when the Gd content is less than 2.5 wt% [19-21].

Considering biosafety, the Gd content in such biodegradable Mg alloy should be low. To date, a very few works have been done on the effects of minor Gd alloying on the microstructures, mechanical properties and corrosion behavior of as-extruded Mg-Zn-Zr based alloys, especially on those with prior solid solution treatment. Herein, in this paper, Mg-1.8Zn-0.5Zr-xGd ( $x=0, 0.5, 1.0, 1.5, 2.0, 2.5$  wt%) alloys were prepared by solid solution treatment and hot extrusion. The microstructure, mechanical properties and corrosion behavior as a function of Gd content were systematically investigated. It is hoped that our research will benefit the general bioimplant material designs beyond the invention of Mg alloys and their engineering design strategies.

## **2. Experimental**

### **2.1 Materials**

Mg-1.8Zn-0.5Zr-xGd alloys were prepared by melting Mg (99.9 wt%), Zn (99.9 wt%), and Mg-30Zr (wt%) and Mg-20Gd (wt%) master alloys in an electric induction furnace then casting [22]. The as-cast ingots were solution-treated at 480 °C for 6 h, and then extruded at 360 °C with an extrusion speed of 5 mm/s and an extrusion ratio of 8. All the extruded rods were then subjected to stress relief annealing at 200 °C for 4 h. Hereafter, these as-extruded Mg-1.8Zn-0.5Zr-xGd ( $x=0, 0.5, 1.0, 1.5, 2.0, 2.5$  wt.%) alloys were donated as E<sub>s</sub>0, E<sub>s</sub>0.5, E<sub>s</sub>1.0, E<sub>s</sub>1.5, E<sub>s</sub>2.0 and E<sub>s</sub>2.5, respectively.

### **2.2 Microstructure and mechanical property determination**

The specimens for microstructure observation were cut parallel to the extrusion direction (ED). Microstructure characterizations were performed by an optical microscope (OLYMPUS, PMG3), a scanning electron microscope (SEM, JSM-7800F) equipped with energy dispersive X-ray spectrometer (EDS) and a transmission electron microscope (TEM, JEM-2100). Sample preparation were carried out the same way as those described in our previous work [23]. Tensile specimens having a gauge length of 25 mm and a diameter of 5 mm were machined

from the as-extruded rods parallel to the ED. Tensile tests were conducted by using an AG-1250KN (SHIMADZU) machine under a tensile speed of 1 mm/min.

### 2.3 Corrosion tests

The corrosion rate of these selected alloys was evaluated by measuring the weight loss during immersion test in simulated body fluid (SBF) solution [24] at 37 °C. The SBF solution was refilled every 8 h to keep a constant pH value. After the immersion test, the corrosion products were removed using a 200 g/L CrO<sub>3</sub>+10 g/L AgNO<sub>3</sub> solution. The average corrosion rate was calculated using the following equation [25].

$$P_w = 8.76 \times 10^4 \times \Delta w / At\rho \quad (1)$$

where,  $P_w$  is the corrosion rate (mm/y),  $\Delta w$  the mass loss (g),  $A$  the specimen surface area exposed to the SBF solution (cm<sup>2</sup>),  $t$  the immersion time (hour) and  $\rho$  the density of the alloy (g/cm<sup>3</sup>), respectively.

For electrochemical test, cylindrical samples were mounted into epoxy resin with a surface area of 1 cm<sup>2</sup> exposed to the SBF solution. Potentiodynamic polarization curve and electrochemical impedance spectroscopy (EIS) measurements were carried out at 37 °C using an electrochemical workstation (Autolab PGSTAT128N) to reveal the corrosion behavior of Mg-1.8Zn-0.5Zr-xGd alloys. The chosen alloys, a saturated calomel electrode and graphite sheet were used as working, reference and counter electrode, respectively. Prior to the electrochemical tests, the samples were soaked in the SBF solution for 1 h to achieve equilibrium. The polarization curves were acquired by scanning from -0.25 V to +0.4 V vs. the open circuit potential (OCP) at a scan rate of 1 mV/s. The EIS measurements were carried out at OCP using an AC amplitude of 10 mV in the frequency range from 10 kHz to 0.1 Hz.

X-ray photoelectron spectroscopy (XPS) was used to analyze the chemical composition of corrosion products formed on the surface of E<sub>s</sub>1.5 alloy after SBF immersion for 16, 48, and 120 h. XPS measurements were performed on a Thermo Fisher Scientific ESCALAB 250Xi XPS spectrophotometer. The core-level 1s peak of the adventitious carbon is employed for the overall energy calibration. Mg 1s and Ca

2p spectra were measured and fitted.

### 3. Results

#### 3.1 Microstructure evolution

Fig. 1 shows the optical images of the as-extruded Mg-1.8Zn-0.5Zr-xGd alloys. The near-equiaxed grain structures shown in the images indicate the occurrence of complete dynamic recrystallization (DRX) during hot-extrusion. The average grain size of the alloy without Gd is measured to be about 17.9  $\mu\text{m}$ . With the addition of Gd, one can see a bimodal grain structure in the alloys: coarse grains and fine grains distributed in prior deformation bands along ED. Average grain sizes of these alloys are estimated to be about 9.6  $\mu\text{m}$ , 7.5  $\mu\text{m}$ , 7.3  $\mu\text{m}$ , 7.2  $\mu\text{m}$ , and 6.8  $\mu\text{m}$  from 0.5 to 2.5 wt% Gd, respectively. More second-phase particles are found to distribute along ED in the alloys with high Gd content (2.0, 2.5 wt%).

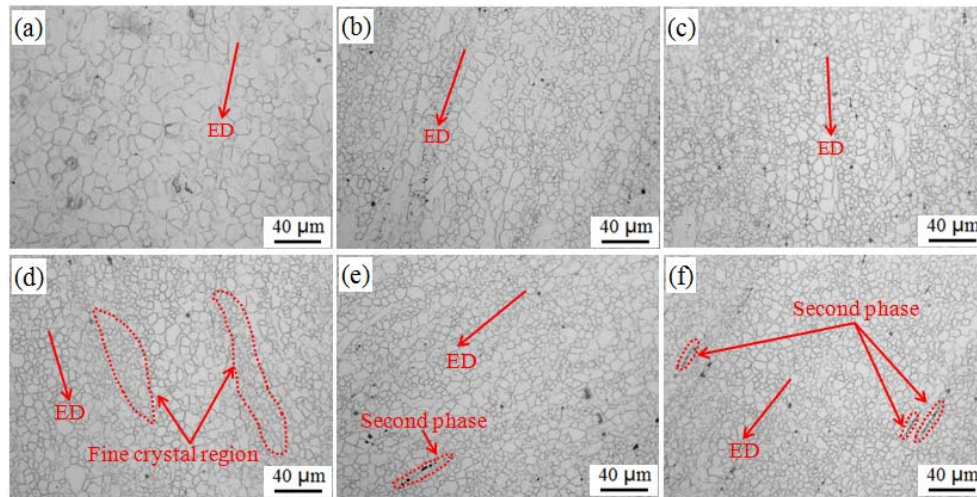


**Fig. 1.** Optical micrographs of the as-extruded Mg-1.8Zn-0.5Zr-xGd alloys: (a)  $E_s0$ ; (b)  $E_{s0.5}$ ; (c)  $E_{s1.0}$ ; (d)  $E_{s1.5}$ ; (e)  $E_{s2.0}$ ; (f)  $E_{s2.5}$ , respectively.

Fig. 2 gives the TEM characterization results of  $E_{s1.5}$  alloy. Fig. 2(a) reveals the presence of subgrains and a small amount of nanoscale second-phase particles that disperse mainly along the DRXed (sub)grain boundaries. The selected area electron diffraction (SAED) pattern of particle A reveals that the particles have a face-centered cubic crystal structure. Interplanar spacings are 0.4219 nm, 0.2197 nm, and 0.2581 nm, which can be indexed to the  $(1\bar{1}\bar{1})$ ,  $(31\bar{1})$  and  $(220)$  planes of  $\text{Mg}_3\text{Gd}$  phase. EDS spectrum in Fig. 2(b) shows that the particles are composed of Mg, Zn and Gd, suggesting a  $(\text{Mg}, \text{Zn})_3\text{Gd}$  phase with Zn dissolved in  $\text{Mg}_3\text{Gd}$ . This finding is in

agreement with other Zn and Gd containing Mg alloys [26].

Second-phase particles with a rectangular-shaped cross section are also found in the Mg matrix (Fig. 2(c)). EDS spectrum in Fig. 2(d) shows that the particles are composed of Mg and Zn. It should be noted there are also some lath-shaped fine structures (marked by C) in Fig. 2(e) showing a relatively weak contrast to the Mg matrix. HR-TEM image in Fig. 2(f) shows a distorted lattice implying the segregation of alloying elements with a different lattice constant other than Mg. These laths might be the nucleation sites of the second-phase precipitates [27]. By the fast Fourier transform (FFT) of the HRTEM image in Fig. 2(g), the second-phase particle is detected to have a primitive cube crystal structure. The interplanar spacings of 0.2711 nm, 0.1969 nm and 0.2857 nm have a good correspondence with those of  $(013)_z$ ,  $(313)_z$  and  $(300)_z$  planes of  $Mg_2Zn_{11}$  phase with  $[03\bar{1}]_z$  zone axis parallel to the electron beam. Considering the chemical compositions in Fig. 2(d), it can be concluded that the particle is  $Mg_2Zn_{11}$ . Fig. 2(i, j) show the HRTEM and FFT image of Mg matrix adjacent to the  $Mg_2Zn_{11}$  particle, respectively. It is found that the  $[010]_\alpha$  zone axis of hcp Mg is parallel to the electron beam. Accordingly, the results demonstrate that the orientation relationship between nano-scale  $Mg_2Zn_{11}$  phase and Mg matrix is  $(013)_z // (002)_\alpha$ ,  $(313)_z // (102)_\alpha$  and  $(300)_z // (100)_\alpha$ . The lattice mismatch ( $\delta$ ) of phase interface can be calculated by [28]:

$$\delta = 2(X_A - X_B) / (X_A + X_B) \quad (2)$$

where,  $X_A$  and  $X_B$  are the interplanar distance of corresponding parallel plane pairs. The calculation results in the lattice mismatch of  $(013)_z // (002)_\alpha$ ,  $(313)_z // (102)_\alpha$ , and  $(300)_z // (100)_\alpha$  are 0.039, 0.035 and 0.027, respectively, implying that the nano-sized  $Mg_2Zn_{11}$  particles have a coherent interfacial relationship with the neighboring  $\alpha$ -Mg matrix.



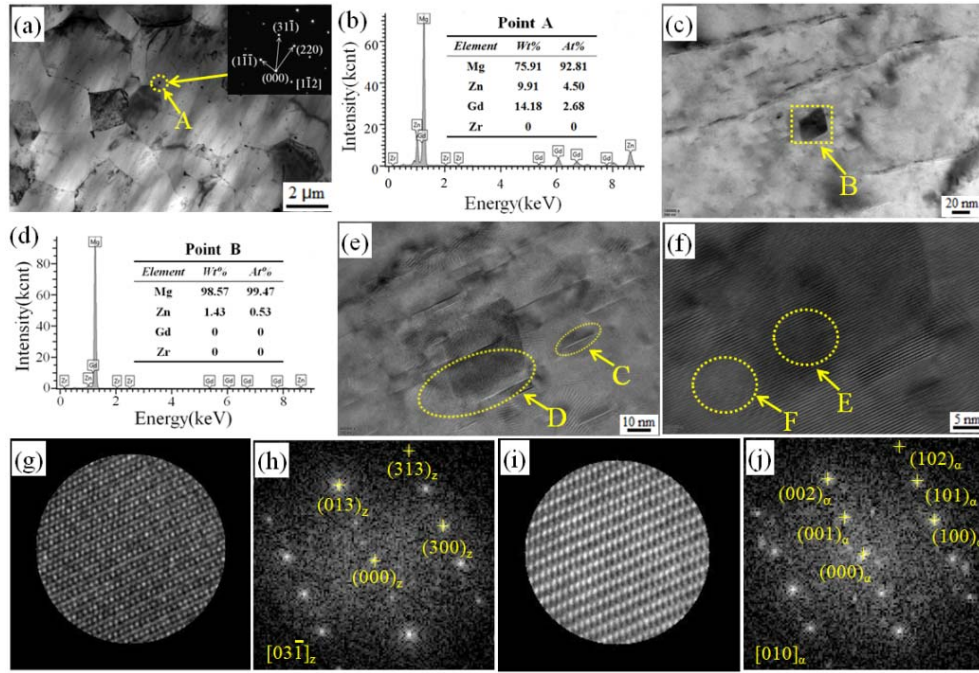


**Fig. 2.** TEM characterizations of second-phase particles in the  $E_s1.5$  alloy. (a) BF-TEM image, SAED of particle A, inset of (a); (b) EDS spectrum of particle A; (c) BF-TEM image of rectangular shaped particles, (d) EDS spectrum of particle B; (e) enlarged image of area B in (c); (f) HR-TEM image of D area; (g) HR-TEM image of the nano-scale second-phase particle; (h) FFT image of (g); (i) HR-TEM image of the  $\alpha$ -Mg matrix; (j) FFT image of (i).

Fig. 3 shows the TEM image, SAED and EDS spectrum of the second-phase particle distributed in the  $E_s2.5$  alloy. In contrast to the nanoscale particles in the  $E_s1.5$  alloy, the particles in Fig. 3(a) with a size of larger than  $1\ \mu\text{m}$ , clearly, are much coarser and aligned as ‘dashed line’. EDS analysis (Fig. 3(b)) on the particles in the area A indicates that the second-phase particles are mainly composed of three elements: Mg, Zn and Gd. SAED of the particle infers that the particle is similar to the second-phase particle in Fig. 2(a) and belongs to the  $(\text{Mg}, \text{Zn})_3\text{Gd}$  phase. More BF-TEM images (Fig. 3(c) and (d)) reveals the co-existence of rectangular-shaped  $\text{Mg}_2\text{Zn}_{11}$  phase and coarse  $(\text{Mg}, \text{Zn})_3\text{Gd}$  phase (marked as B, C, D). Accordingly, it can be concluded that some  $(\text{Mg}, \text{Zn})_3\text{Gd}$  based particles have not dissolved into the alloy matrix during solid solution treatment and been crushed to smaller pieces during extrusion process.

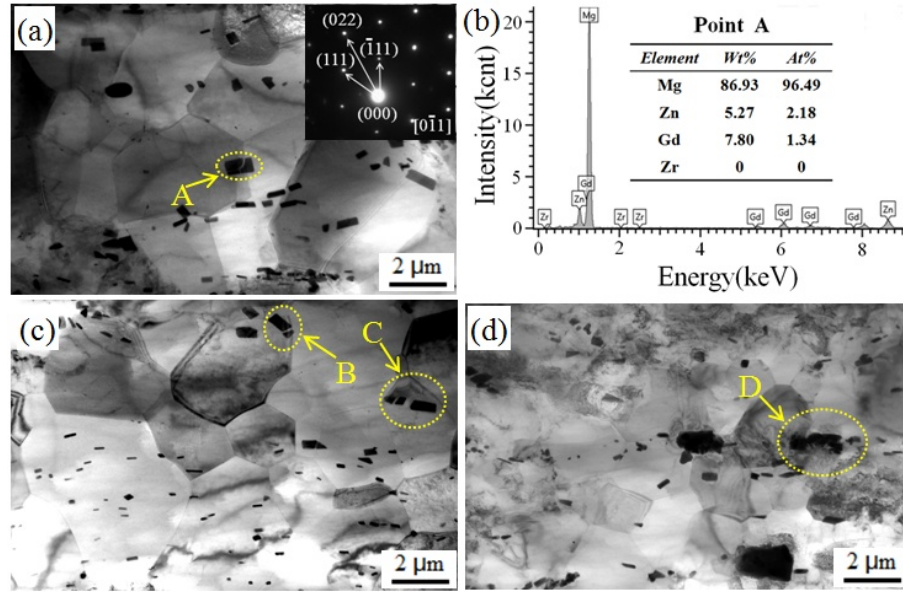


**Fig. 3.** TEM images and corresponding SAED patterns of  $E_s2.5$  alloy.

### 3.2 Mechanical properties and fracture surfaces

The engineering stress-strain curves of as-extruded Mg-1.8Zn-0.5Zr-xGd alloys are plotted in Fig. 4. The UTS, YS and EL values are summarized in Table 1. Impressively, alloying Gd with the Mg-Zn-Zr alloy significantly improves the strength and ductility. The alloy with 2.0 wt% Gd has the best mechanical properties, and its UTS, YS and EL values are  $288.5 \pm 3.0$  MPa,  $257.6 \pm 2.8$  MPa and  $33.5 \pm 1.2\%$ .

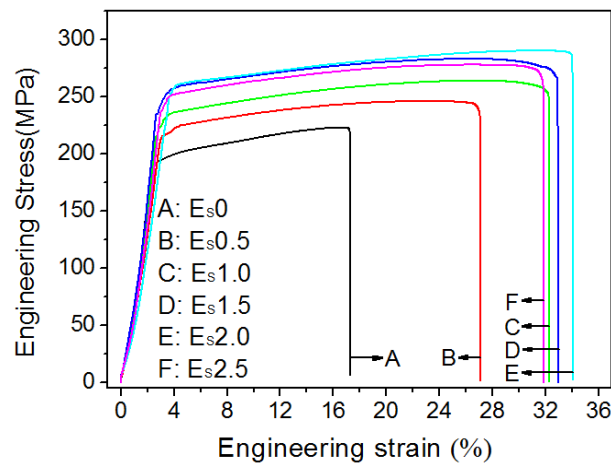


**Fig. 4.** Engineering stress-strain curves of as-extruded Mg-1.8Zn-0.5Zr-xGd alloys.

**Table 1** Mechanical properties of as-extruded Mg-1.8Zn-0.5Zr-xGd alloys.

Material	$E_s0$	$E_s0.5$	$E_s1.0$	$E_s1.5$	$E_s2.0$	$E_s2.5$
----------	--------	----------	----------	----------	----------	----------



UTS (MPa)	228.4±2.7	244.3±2.8	262.6±3.1	280.8±2.9	288.5±3.0	276.7±2.9
YS (MPa)	192.8±2.5	217.7±2.6	233.2±2.8	252.4±2.7	257.6±2.8	248.6±2.7
EL (%)	17.2±0.9	26.7±1.2	32.1±1.1	32.9±1.3	33.5±1.2	31.5±1.3

Fig. 5 shows the fracture surfaces of the extruded Mg-1.8Zn-0.5Zr-xGd alloys after tensile failure. Without Gd, fracture surface of the alloy is characterized of quasi-cleavage fracture together with fine but shallow dimples decorating the surface (Fig. 5(a)). With increasing Gd content to 2.0 wt%, the size and number of dimples gradually increase while the quasi-cleavage fractures gradually decrease until disappear, shifting to more ductile fractures. Second-phase particles with a size of about 1  $\mu\text{m}$  are found in the fracture surface of E<sub>s</sub>2.0 alloy, as marked by the yellow ellipses in Fig. 5(e). When the Gd content increases to 2.5 wt% (Fig. 5(f)), the size of second-phase particles seen in the fracture surface is about 2.5  $\mu\text{m}$ .

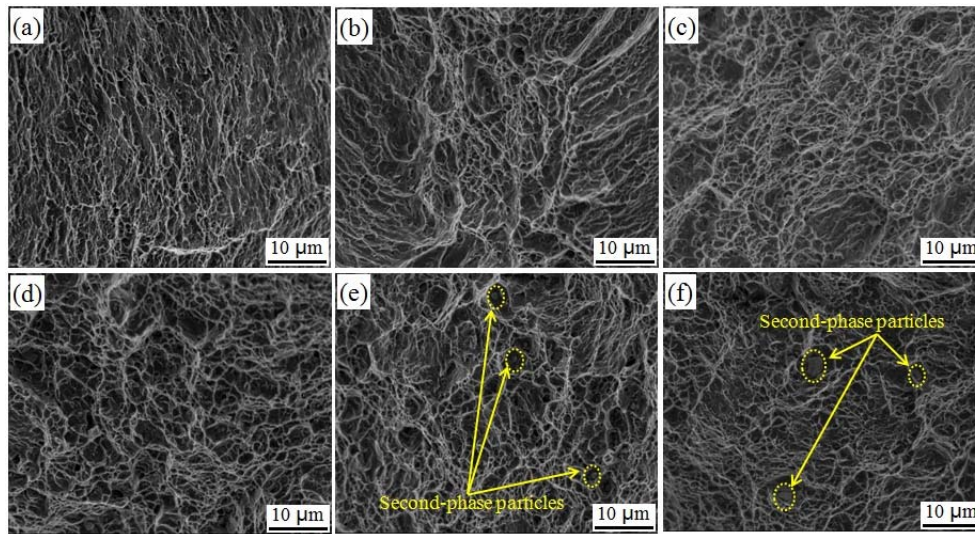


**Fig. 5.** Fracture surfaces of as-extruded (a) E<sub>s</sub>0; (b) E<sub>s</sub>0.5; (c) E<sub>s</sub>1.0; (d) E<sub>s</sub>1.5; (e) E<sub>s</sub>2.0; (f) E<sub>s</sub>2.5 alloy.

### 3.3 Corrosion behavior

Fig. 6(a) shows the polarization curve of the as-extruded Mg-1.8Zn-0.5Zr-xGd alloys measured after 1 h immersion in SBF solution. Table 2 summaries the self-corrosion potential ( $E_{corr}$ ), self-corrosion current density ( $I_{corr}$ ) and corrosion rate ( $P_i$ ) obtained by Tafel extrapolation. In general, alloying Gd with the Mg alloys has a considerable enhancement of the corrosion resistance, evidenced by the more positive

$E_{corr}$ , lower  $I_{corr}$  and  $P_i$ . The alloy with 1.5 wt% Gd owns the lowest  $P_i$ . After 120 h immersion (Fig. 6(b)), the alloy with 1.5 wt% Gd still possesses the lowest  $P_w$  estimated by average weight loss. The  $E_{s1.5}$  alloy could be a promising medical implanting alternative with excellent mechanical properties, corrosion resistance and high biosafety (only 1.5 wt% RE content).

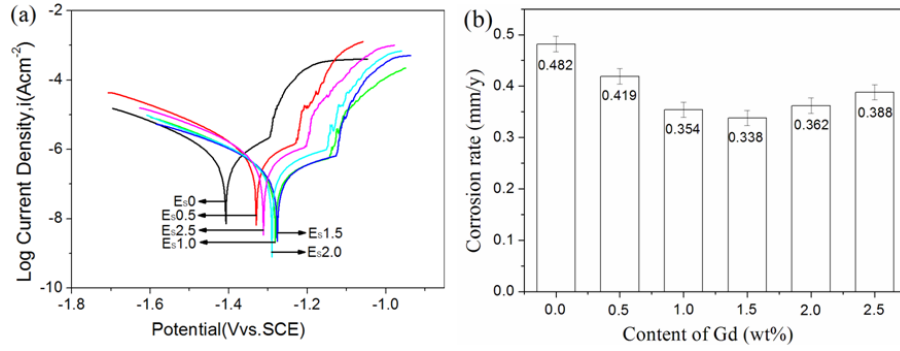


**Fig. 6.** (a) Polarization curves of as-extruded Mg-1.8Zn-0.5Zr-xGd alloys measured after 1 h immersion in SBF solution, and (b)  $P_w$  calculated by weight loss after 120 h immersion in SBF solution.

**Table 2**  $E_{corr}$ ,  $I_{corr}$  and  $P_i$  of as-extruded Mg-1.8Zn-0.5Zr-xGd alloys derived from the polarization curves.

Material	$E_{s0}$	$E_{s0.5}$	$E_{s1.0}$	$E_{s1.5}$	$E_{s2.0}$	$E_{s2.5}$
$E_{corr}$ (Vvs.SCE)	-1.408±0.013	-1.329±0.014	-1.281±0.011	-1.276±0.013	-1.291±0.014	-1.312±0.013
$I_{corr}$ (uA/cm <sup>2</sup> )	3.401±0.012	2.614±0.013	2.482±0.011	2.480±0.012	2.485±0.013	2.221±0.013
$P_i$ (mm/y)	0.154±0.007	0.127±0.008	0.088±0.007	0.086±0.007	0.091±0.008	0.112±0.008

To study the corrosion resistance of  $E_{s1.5}$  alloy, EIS spectra (Nyquist plots, impedance modulus and phase angle of Bode plots) from the  $E_{s1.5}$  alloy after different immersion times in SBF were analyzed, as presented in Fig. 7. Two capacitive loops in high frequency and medium/low frequency are shown in the Nyquist plots. Nevertheless, the loops have different radius. The medium to low-frequency capacitive loop band is usually related to the charge transfer resistance of corrosion layer, while the high-frequency capacitive loop is usually related to the charge transfer resistance of oxide film on the alloy surface [29]. As is known, the

larger the radius of the capacitive loop, the stronger the corrosion resistance of the alloy in the solution [30]. The radius of the high-frequency loop increases with longer immersion times, implying decreased corrosion rate of the alloy with increasing immersion time. Additionally, Fig. 7(d) shows the equivalent circuit model for fitting of the EIS plots, in which  $R_s$  stands for electrolyte resistance between the reference and working electrode,  $R_l$  and  $CPE_l$  are the resistance of  $Mg^{2+}$  through the corrosion layer and double-layer capacitance of the corrosion layer/electrolyte interface.  $R_2$  and  $CPE_2$  are the resistances of MgO barrier film and the double-layer capacitance of substrate/MgO film, respectively. Due to non-uniform current and potential distributions, constant phase element ( $CPE$ ) is employed here to study a non-ideal capacitor deviated from the ideal capacitive behavior at the interfaces [31]. The extracted data are summarized in Table 3.  $R_s$  has a value about 15~30  $\Omega$  in the SBF solution. A rapid increase of  $R_l$  and  $R_2$  can be observed in the first 48 h, corresponding to an increase resistance of the corrosion product layer over time. The  $R_l$  and  $R_2$  increase slowly from 48 h to 96 h, which can be related to the increase thickness of the corrosion product layer. After 96 h, the  $R_l$  and  $R_2$  tend to be stable with prolonged immersion time. This is attributed to the near-dynamic equilibrium of dissolution and generation of corrosion products after renewal of the SBF solution [32].

Fig. 8 shows the  $P_w$  of the E<sub>s</sub>1.5 alloy every 8 h after immersed in SBF solution for 120 h. The  $P_w$  decreases rapidly with increasing immersion time within 48 h firstly, then decreases gradually, and finally achieves a plateau after 96 h immersion, showing a good agreement with the results in Fig. 7 and Table 3.

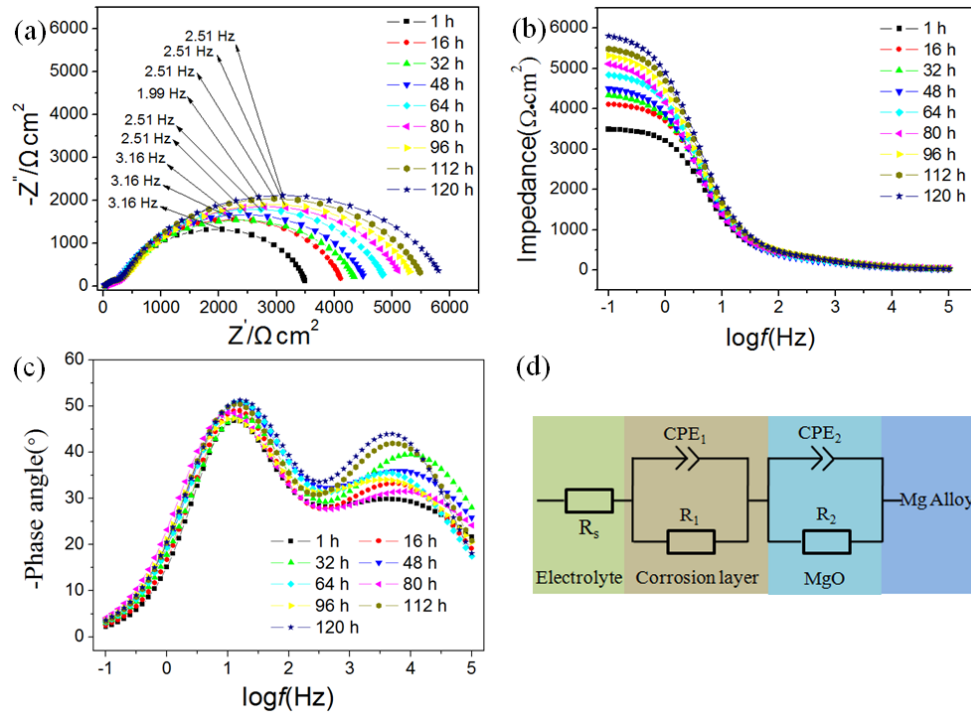


**Fig. 7.** (a) Nyquist plots, (b) impedance vs. frequency and (c) phase angle vs. frequency plots obtained from the EIS measurements for  $E_s1.5$  alloy after different immersion times. (d) equivalent circuit of the EIS spectra of  $E_s1.5$  alloy.

**Table 3** Values obtained from the EIS spectra of  $E_s1.5$  alloy after different immersion time in SBF solution.

Time (h)	$R_s$ ( $\Omega$ )	$R_l$ ( $\text{k}\Omega \cdot \text{cm}^2$ )	$CPE_l$ ( $\Omega^{-1} \cdot \text{cm}^{-2} \cdot \text{s}^{-n}$ )	$n_1$	$R_2$ ( $\Omega \cdot \text{cm}^2$ )	$CPE_2$ ( $\Omega^{-1} \cdot \text{cm}^{-2} \cdot \text{s}^{-n}$ )	$n_2$
1	25.2	3.06	20.8	0.896	434	31.9	0.491
16	26.2	3.79	19.4	0.872	335	17.6	0.614
32	17.4	4.10	21.9	0.822	303	21.6	0.636
48	18.6	4.25	21.9	0.845	308	32.2	0.563
64	28.2	4.61	20.0	0.841	319	26.1	0.632
80	23.1	4.84	25.3	0.832	372	33.2	0.524
96	28.8	4.95	22.1	0.834	405	28.5	0.554
112	23.6	5.22	18.7	0.844	418	17.8	0.692
120	23.1	5.63	18.6	0.821	386	16.3	0.732

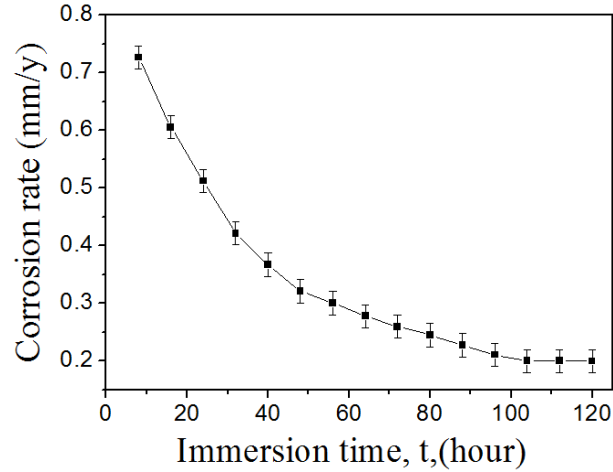


**Fig. 8.**  $P_w$  for  $E_s1.5$  alloy immersed in SBF solution for 120 h.

The corrosion morphologies of the  $E_s1.5$  alloy after immersion for 16 h, 32 h, 48 h and 120 h were characterized by SEM and shown in Fig. 9. Corresponding macroscopic images after the removal of corrosion products are also shown as the inset images. After 16 h immersion (inset of Fig. 9(a)), the alloy surface is relatively uniform and shows no trace of local corrosion. EDS analysis shows that the corrosion layer is mainly composed of O, Mg, P, Ca, Gd and Zn (Table 4). With increasing immersion time, line-like corrosion areas began to appear (inset of Fig. 9(b)) and then became wider (inset of Fig. 9(c)). The area with corrosion products increase until the corrosion products covers the entire alloy surface after 120 h immersion (inset of Fig. 9(d)). Meanwhile, the thickness of corrosion product layer and the width of cracks forming in the corrosion layer increases gradually. The as-observed cracks are mainly caused by the dehydration in the water-containing corrosion layer during drying [33]. Signals of Gd and Zn in the EDS spectra disappear, while the main elements in the corrosion layer are detected to be O, Mg, P and Ca. At the same time, it can also be noted that there is only a slight difference of compositions at the white corrosion product (D) and the dense black corrosion product (E) in Fig. 9(d) and Table 4.

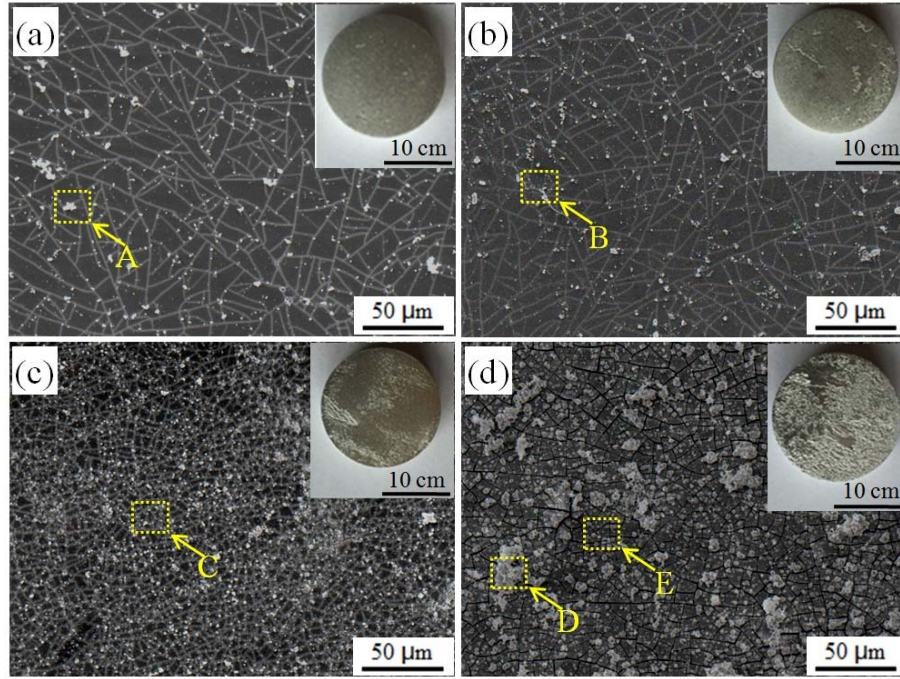


**Fig. 9.** SEM images of  $E_s1.5$  alloy surfaces after immersion in SBF solution for: (a) 16 h; (b) 32 h; (c) 48 h; (d) 120 h. The inset images are optical images of the surfaces after removing corrosion products.

**Table 4** EDS analyses (as marked in Fig. 9) of  $E_s1.5$  alloy surface after different immersion time in SBF solution.

Position	Mass fraction/%					
	O	Mg	P	Ca	Gd	Zn
A	40.02	18.47	16.72	16.52	1.21	1.06
B	42.05	10.84	22.41	2.41	0.92	0.38
C	25.42	46.91	14.86	12.81	0	0
D	52.26	4.84	17.55	25.35	0	0
E	37.56	6.49	24.09	31.86	0	0

XPS spectra were acquired for the Mg 1s and Ca 2p regions after SBF immersion for different times. As shown in Fig. 10(a), the alloy surface is composed of Mg and MgO before SBF immersion, as determined by the Mg 1s binding energies at 1303.9 eV and 1306.3 eV, respectively [34]. After 16 h immersion, the Mg 1s spectra show the presence of  $Mg(OH)_2$  and MgO. An emerging peak at 1309.4 eV, corresponding to



Mg 1s in the  $(\text{Ca, Mg})_3(\text{PO}_4)_2$  [35], can be seen which can be ascribed to attaching, absorbing or reaction of the SBF with the alloy's metallic surface. Such a phosphate becomes dominating after 48 h immersion. After 120 h immersion, the corrosion product is composed of  $\text{Mg}(\text{OH})_2$ ,  $\text{MgO}$ ,  $(\text{Ca, Mg})_3(\text{PO}_4)_2$  as well as a small portion of Mg metal which is mostly due to XPS probabtion depth and peeling off of corrosion product [36].

Fig. 10(b) shows the Ca 2p XPS spectra, in which the calcium compounds are seen to form gradually on the  $\text{E}_s1.5$  surface. The calcium attachment onto the surface is rather weak after 16 h immersion, as evidenced by a very low Ca 2p spectra compared with the Mg KLL Auger spectra arisen from the Mg. However, after longer immersion, the overall Ca content increases as denoted from the XPS intensities. The  $\text{Ca}_{10}(\text{PO}_4)_6(\text{OH})_2$  is formed along with the  $(\text{Ca, Mg})_3(\text{PO}_4)_2$ , as shown in Ca-48h and Ca-120h spectra. Taking the Mg Auger as the reference, the surface content of  $\text{Ca}_{10}(\text{PO}_4)_6(\text{OH})_2$  increases with the immersion time and against the Mg content. It is worth mentioning that the  $\text{Ca}_{10}(\text{PO}_4)_6(\text{OH})_2$  is the well-known key composite of the dental enamel and dentin, whose presence indicates a good biocompatibility of the alloy.

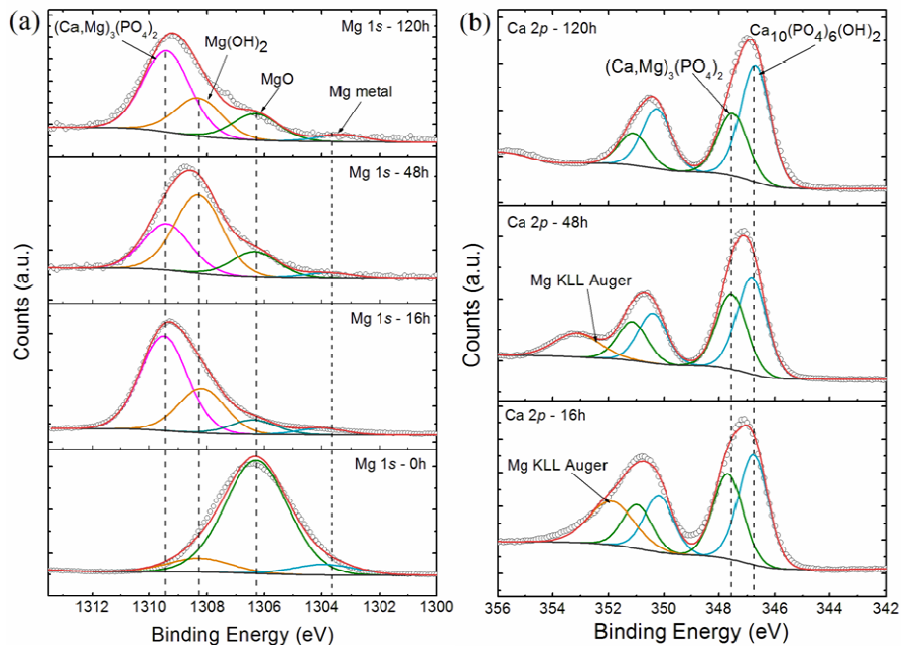


**Fig. 10.** (a) Mg 1s and (b) Ca 2p XPS spectra of the  $\text{E}_s1.5$  alloy recorded after different immersion times in SBF solution.

## 4. Discussions

### 4.1 Effect of Gd alloying on microstructure evolution and mechanical properties

The grain size of DRXed magnesium alloys during hot-extrusion depend on the chemical composition, distribution and size of the second-phase particles with the alloy [37]. As shown in Fig. 1, the grains are remarkably refined by Gd alloying. Comparison of the distribution and size of second-phase particles, particularly the  $(\text{Mg}, \text{Zn})_3\text{Gd}$  phase shown in Fig. 2 and 3, indicates that the solubility of Gd in the Mg-1.8Zn-0.5Zr alloy matrix is about 1.5 wt% at the applied solid solution treatment temperature. Gd solutes can effectively reduce the stacking fault energy of Mg alloys [38]. The smaller the stacking fault energy is, the higher stored energy can be during plastic deformation [39]. The high stored energy by Gd alloying could promote the nucleation rate and the number of nuclei to accelerate DRX [40]. Thus, a remarkable grain refinement can be achieved by as less as 0.5 wt% Gd alloying. Consequently, a significant improvement of mechanical property is obtained, which can be explained by the Hall-Petch equation [41]. The increasing amount of Gd solutes also contribute to improved strengths (Fig. 4 and Table 1), namely, solid solution strengthening [42]. Meanwhile, Gd dissolved in the alloy matrix can activate more non-basal slip systems during extrusion [43]. These non-basal slip systems promote the formation of mobile dislocations, reduce deformation resistance and work hardening of Mg alloys [44]. Additionally, the refined grains also lead to limited stress concentration and twinning formation [45], thereby improving the plasticity of Gd containing alloy.

The increasing of Gd content leads to also the precipitation of the  $(\text{Mg}, \text{Zn})_3\text{Gd}$  phase that precipitate out concurrently with DRX (Fig. 2). The dispersed fine precipitates, including the  $\text{Mg}_2\text{Zn}_{11}$ , have a pinning effect, to inhibit the migration of grain boundaries and to hinder grain growth during DRX [46], which also results in grain refinement. Nanoscale precipitates that have a coherent interfacial relationship with the alloy matrix hinder the movement of dislocations during the tensile process to improve the mechanical properties [47-50]. These are evidenced by the transition to more ductile fracture (Fig. 5) and increasing UST, YS and EL with increasing Gd content until 2.0 wt%.

When the Gd content equals 2.5 wt%, non-dissolved and retained (Mg, Zn)<sub>3</sub>Gd break into micron-sized rod-like particles (~2 μm) in the alloy. These particles usually have a non-coherent interface with the alloy matrix, meaning a weak atomic bonding force with the alloy matrix [51]. During the tensile process, the particles usually become the source of crack initiation and propagation channels [52], which accelerates the fracture and reduces the mechanical properties of the 2.5 wt% Gd containing alloy.

#### 4.2 Influence of Gd alloying on corrosion behavior

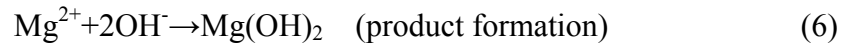
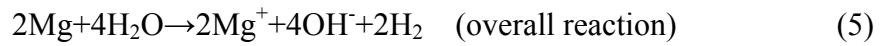
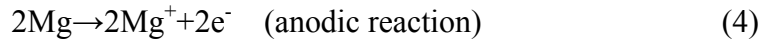
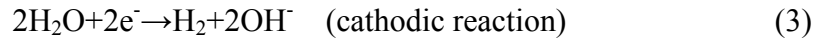
It has been reported that the Gd solutes in Mg alloys can promote the formation of a dense oxide protective film on the surface, which can reduce the cathodic current density and improve the corrosion resistance of the alloy [53-54]. We found that as the Gd content increases (<1.5 wt%), the  $E_{corr}$  of the alloy gradually move positively, meaning the corrosion resistance of the alloy is enhanced. Meanwhile, grain refinement has also been reported to improve corrosion resistance of the alloy [55]. With in increasing Gd, the grain size decreases, and the corrosion resistance increases. The enhanced corrosion resistance can be due to that the finer the grains, the more conducive to the formation of a dense and continuous oxide protective film on the alloy surface. Meanwhile, the refined grain structure can also reduce the discontinuity between the oxide protective film and the alloy [56]. Hence, the oxide protective film can effectively prevent the corrosive medium from penetrating into the alloy matrix.

When the Gd content is greater than 1.5 wt%, the grain size decreases slowly, and the number and size of the second-phase particles in the alloy increase with increasing Gd. These second-phase particles usually act as the cathode and cause galvanic corrosion to the surrounding α-Mg matrix. Increasing size of second-phase particles increase the power of galvanic corrosion with the surrounding α-Mg matrix, accelerate the dissolution of the matrix, and therefore reduce the corrosion resistance of the alloy. The second-phase particles can fall off too which leads to an increase of the corrosion rate [57]. Therefore, a gradual decrease in the corrosion resistance of the alloy when the Gd content is in the range of 1.5 to 2.5 wt%.

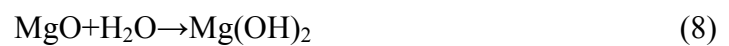
#### 4.3 Corrosion mechanism

It is noteworthy that the corrosion of Mg is a complex process and different mechanisms have been proposed [58-59]. In the E<sub>s</sub>1.5 alloy, fine DRX grains containing subgrains are clustered and distributed along the ED (Fig. 1(d)). In Mg alloys, these areas that contain high-density dislocations are usually acted as anodes during corrosion and preferentially corrode [60]. Therefore, as the immersion time increases, the number and width of the strip-shaped corrosion zone on the alloy surface gradually increase. The immersion, electrochemical and surface analysis demonstrate that the corrosion resistance of the E<sub>s</sub>1.5 alloy is the best among the other alloys, which is due to the grain refinement and the formation of fine second-phase particles. According to the microstructures, XPS, EIS and  $P_w$  results, the corrosion mechanism of the E<sub>s</sub>1.5 alloy in the SBF solution is schematically summarized in Fig. 11. The corrosion process undergoes three distinct stages as follows.

Stage 1 Hydroxidation (0-48 h), Fig. 11(a): chemical reactions between the Mg matrix and water dominates. The corrosion of E<sub>s</sub>1.5 alloy in SBF occurs through the following partial reactions:



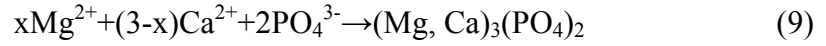
The corrosion product layer of Mg(OH)<sub>2</sub> were gradually thickened with immersion time, and the alloy surface exposed to SBF gradually decreased. As a result,  $R_{p1}$  and  $R_{p2}$  in EIS rapidly increased, and corrosion rate declined rapidly. The corrosion layer became thicker with time, and inhibited the SBF's penetration into the matrix. Therefore, the reaction that involves the fresh-produced and native MgO layers is also possible:



Side reactions at this stage may also happen through e.g.,  $x\text{Mg}^{2+} + (3-x)\text{Ca}^{2+} + 2\text{PO}_4^{3-}$  to form a certain amount of (Mg, Ca)<sub>3</sub>(PO<sub>4</sub>)<sub>2</sub>. However, the Ca attachment to the matrix is rather low as shown in Fig. 10(b), leading to relative

smaller reaction rates compared to hydroxidation.

Stage 2 Phosphatization and hydroxidation (48-96 h), Fig. 11(b). The thickness of  $\text{Mg}(\text{OH})_2$  corrosion layer and the concentration of  $\text{Mg}^{2+}$  in SBF gradually increase. A compact mixture of  $\text{Mg}(\text{OH})_2$ ,  $(\text{Ca}, \text{Mg})_3(\text{PO}_4)_2$  and  $\text{Ca}_{10}(\text{PO})_4(\text{OH})_2$  corrosion products has formed, as verified by the XPS (Fig. 10) and EDS results (Fig. 9) in Sec.3.3. With increasing immersion time, the continuous thickening of the corrosion layer led to the  $R_{p1}$  and  $R_{p2}$  gradually increase. Therefore, the corrosion rate of the alloy decreased, which was beneficial to the overflow of the generated  $\text{H}_2$  through the corrosion layer [61-62]. The reactions are as follows.



Stage 3 Equilibrium (96-120 h), Fig. 11(c). During the renewal cycles of the SBF, the formation and dissolution of corrosion products reached a dynamic equilibrium, resulting in small changes in  $R_{p1}$  and  $R_{p2}$ . The alloy surface is covered by the  $\text{MgO}$ ,  $\text{Mg}(\text{OH})_2$ ,  $(\text{Ca}, \text{Mg})_3(\text{PO}_4)_2$  compounds as well as a bio-preferable  $\text{Ca}_{10}(\text{PO})_4(\text{OH})_2$ .

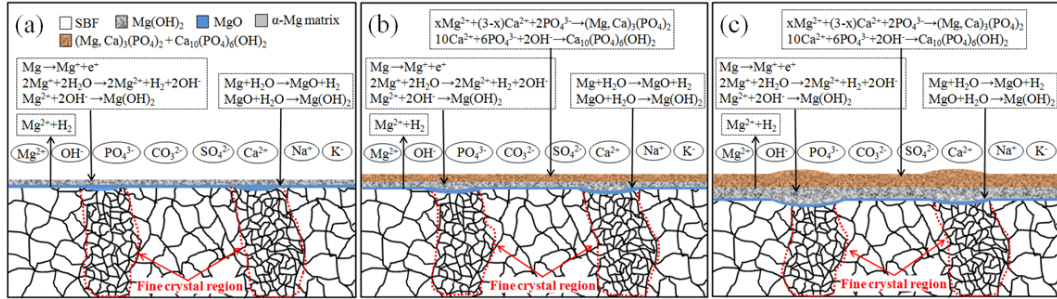


**Fig. 11.** The corrosion process of E<sub>5.1.5</sub> alloy in SBF solution: (a) First stage; (b) Second stage; (c) Third stage.

## 5. Conclusions

In conclusion, we systematically studied the effects of Gd alloying on the microstructure, mechanical properties, and corrosion resistance of solid-solution Mg-1.8Zn-0.5Zr alloys. The main conclusions are as follows.

1. The grains of the extruded Mg-1.8Zn-0.5Zr-xGd alloy are significantly refined by the Gd alloying. A small amount of nanoscale  $(\text{Mg}, \text{Zn})_3\text{Gd}$  particles and  $\text{Mg}_2\text{Zn}_{11}$  particles that have a coherent interface with the matrix have precipitated out in the

alloy with 1.5 wt% Gd.

2. For Gd less than 1.5 wt%, the enhanced mechanical properties of the alloy are mainly due to the grain refinement and Gd solutes strengthening. With precipitated nanoscale  $(\text{Mg, Zn})_3\text{Gd}$  and  $\text{Mg}_2\text{Zn}_{11}$  particles for Gd in the range of 1.5-2.0 wt%, the mechanical properties of the alloy can be further improved. The alloy with 2.0 wt% Gd has the best mechanical properties: UTS of 288.5 MPa, YS of 257.6 MPa and EL of 33.5%, as compared with that without Gd alloying: UTS of 228.4 MPa, YS of 192.8 MPa and EL of 17.2 %.

3. The refined grains of the alloys by Gd alloying result in increasing corrosion resistance as the Gd content increases to 1.5 wt%. For Gd content greater than 1.5 wt%, the increase in the size and number of the second-phase particles causes the corrosion resistance of the alloy to decrease. The  $\text{E}_{\text{s}1.5}$  alloy, i.e. the alloy with 1.5 wt% Gd, has the best corrosion resistance.

4. The corroded surface analysis of the  $\text{E}_{\text{s}1.5}$  alloy demonstrates three different stages of the corrosion process: The rapid increase of  $\text{Mg}(\text{OH})_2$  on the surface leads to a rapid decrease in the corrosion rate at the initial stage. Then the dense  $\text{Mg}(\text{OH})_2$ ,  $(\text{Ca, Mg})_3(\text{PO}_4)_2$ ,  $\text{Ca}_{10}(\text{PO})_4(\text{OH})_2$  corrosion layer leads to a slow decrease in the corrosion rate. Finally, the formation and dissolution of corrosion products reach a dynamic equilibrium and the corrosion rate becomes stable.

5. Regarding the improvement of mechanical properties and corrosion behaviors, the extruded  $\text{Mg-1.8Zn-0.5Zr}$  alloy with 1.5-2.0 wt% Gd alloying can be considered to be a promising candidate of usage as biodegradable implant materials.

### **Acknowledgements**

This work was supported by the Education Department of Henan Province (20A430010), the National Natural Science Foundation of China (U1804146, 52111530068). Foreign Experts and Introduction Project of Henan Province (HNGD2020009). Financial supports from profile grant of the Academy of Finland (No. 311934). The Center of Microscopy and Nanotechnology at University of Oulu is thanked for the XPS characterizations.

### **Conflict of Interest**



The authors declare no conflict of interest.

## References

- [1] Y.X. Liu, M. Curioni, Z. Liu, Correlation between electrochemical impedance measurements and corrosion rates of Mg-1Ca alloy in simulated body fluid, *Electrochim. Acta.* 264 (2018) 101-108.
- [2] D. Mareci, G. Bolat, J. Izquierdo, C. Crimu, C. Munteanu, I. Antoniac, R.M. Souto, Electrochemical characteristics of bioresorbable binary MgCa alloys in Ringer's solution: Revealing the impact of local pH distributions during in-vitro dissolution, *Mater. Sci. Eng. C* 60 (2016) 402-410.
- [3] Y.C. Wan, S.Y. Xu, C.M. Liu, Y.H. Gao, S.N. Jiang, Z.Y. Chen, Enhanced strength and corrosion resistance of Mg-Gd-Y-Zr alloy with ultrafine grains, *Mater. Lett.* 213 (2018) 274-277.
- [4] X.N. Gu, Y.F. Zheng, S.P. Zhong, T.F. Xi, J.Q. Wang, W.H. Wang, Corrosion of, and cellular responses to Mg-Zn-Ca bulk metallic glasses, *Biomaterials* 31 (2010) 1093-1103.
- [5] R.C. Zeng, W. Ke, Y.B. Xu, E.H. Han, Z.Y. Zhu, Recent development and application of magnesium alloys, *Acta. Metall. Sin.* 37 (2001) 673-685.
- [6] X.N. Gu, N. Li, Y.F. Zheng, L.Q. Ruan, In vitro degradation performance and biological response of a Mg-Zn-Zr alloy, *Mater. Sci. Eng. B* 176 (2011) 1778-1784.
- [7] X.B. Zhang, Z.X. Ba, Q. Wang, Y.J. Wu, Z.Z. Wang, Q. Wang, Uniform corrosion behavior of GZ51K alloy with long period stacking ordered structure for biomedical application, *Corros. Sci.* 88 (2014) 1-5.
- [8] Z.Q. Zhang, X. Liu, W.Y. Hu, J.H. Li, Q.C. Le, L. Bao, Z.J. Zhu, J.Z. Cui, Microstructures, mechanical properties and corrosion behaviors of Mg-Y-Zn-Zr alloys with specific Y/Zn mole ratios, *J. Alloys. Compd.* 624 (2015) 116-125.
- [9] J.Y. Zhang, Z.X. Kang, L.L. Zhou, Microstructure evolution and mechanical properties of Mg-Gd-Nd-Zn-Zr alloy processed by equal channel angular processing, *Mater. Sci. Eng. A* 647 (2015) 184-190.
- [10] S. Gollapudi, Grain size distribution effects on the corrosion behaviour of

materials, Corros. Sci. 62 (2012) 90-94.

- [11] X.B. Zhang, Z.X. Ba, Z.Z. Wang, Y.J. Wu, Y.J. Xue, Effect of LPSO Structure on mechanical properties and corrosion behavior of as-extruded GZ51K magnesium alloy, Mater. Lett. 163 (2016) 250-253.
- [12] F.Y. Cao, Z.M. Shi, G.L. Song, M. Liu, M.S. Dargusch, A. Atrens, Influence of hot rolling on the corrosion behavior of several Mg-X alloys, Corros. Sci. 90 (2015) 176-191.
- [13] K. Liu, J.H. Zhang, L.L. Rokhlin, F.M. Elkin, D.X. Tang, J. Meng, Microstructures and mechanical properties of extruded Mg-8Gd-0.4Zr alloys containing Zn, Mater. Sci. Eng. A 505 (2009) 13-19.
- [14] X.B. Zhang, G.Y. Yuan, L. Mao, J.L. Niu, W.J. Ding, Biocorrosion properties of as-extruded Mg-Nd-Zn-Zr alloy compared with commercial AZ31 and WE43 alloys, Mater. Lett. 66 (2012) 209-211.
- [15] H. Yao, J.B. Wen, Y. Xiong, Y. Lu, M. Huttula, Microstructure Evolution in Mg-Zn-Zr-Gd Biodegradable Alloy: The Decisive Bridge Between Extrusion Temperature and Performance, Front. Chem. 6 (2018) 71.
- [16] H. Huang, G.Y. Yuan, C.L. Chen, W.J. Ding, Z.C. Wang, Excellent mechanical properties of an ultrafine grained quasicrystalline strengthened magnesium alloy with multi-modal microstructure, Mater. Lett. 107 (2013) 181-184.
- [17] S.D. Wang, D.K. Xu, X.B. Chen, E.H. Han, C. Dong, Effect of heat treatment on the corrosion resistance and mechanical properties of an as-forged Mg-Zn-Y-Zr alloy, Corros. Sci. 92 (2015) 228-236.
- [18] H.W. Miao, H. Huang, Y.J. Shi, H. Zhang, J. Pei, G.Y. Yuan, Effects of solution treatment before extrusion on the microstructure, mechanical properties and corrosion of Mg-Zn-Gd alloy in vitro, Corros. Sci. 122 (2017) 90-99.
- [19] J.M. Seitz, A. Lucas, M. Kirschenr, Magnesium-based compression screws: a novelty in the clinical use of implants, Jom. 68 (2016) 1177-1181.
- [20] J.C. Bousquet, S. Sanini, D.D. Stark, P.F. Hahn, M. Nigam, J. Wittenberg, J.T. Ferrucci, Gd-Dota: characterization of a new paramagnetic complex, Radiology 166 (1988) 693-698.

- [21] H. Yao, B.Y. Fang, H.N. Shi, H. Singh, M. Huttula, W. Cao, Microstructures, mechanical properties and degradation behavior of as-extruded Mg-1.8Zn-0.5Zr-xGd ( $0 \leq x \leq 2.5$  wt%) biodegradable alloys, *J. Mater. Sci.* 56 (2021) 11137-11153.
- [22] H. Yao, J.B. Wen, Y. Xiong, Y. Liu, Y. Lu, W. Cao, Microstructures, Mechanical Properties and Corrosion Behavior of As-Cast Mg-2.0Zn-0.5Zr-xGd (wt%) Biodegradable Alloys, *Materials* 11 (2018) 1564.
- [23] H. Yao, J.B. Wen, Y. Xiong, Y. Lu, F.Z. Ren, W. Cao, Extrusion temperature impacts on biometallic Mg-2.0Zn-0.5Zr-3.0Gd (wt%) solid-solution alloy, *J. Alloys. Compd.* 739 (2018) 468-480.
- [24] M. Ascencio, M. Pekguleryuz, S. Omanovic, An investigation of the corrosion mechanisms of WE43 Mg alloy in a modified simulated body fluid solution: The effect of electrolyte renewal, *Corros. Sci.* 91 (2015) 297-310.
- [25] J.L. Li, L.L. Tan, P. Wan, X.M. Yu, K. Yang, Study on microstructure and properties of extruded Mg-2Nd-0.2Zn alloy as potential biodegradable implant material, *Mater. Sci. Eng. C* 49 (2015) 422-429.
- [26] J. Liu, L.X. Yang, C.Y. Zhang, B. Zhang, T. Zhang, Y. Li, K.M. Wu, F.H. Wang, Role of the LPSO structure in the improvement of corrosion resistance of Mg-Gd-Zn-Zr alloys, *J. Alloys. Compd.* 782 (2019) 648-658.
- [27] J.A. Österreicher, M. Kumar, A. Schiffl, S. Schwarz, G.R. Bourret, Secondary precipitation during homogenization of Al-Mg-Si alloys: Influence on high temperature flow stress, *Mater. Sci. Eng. C* 687 (2017) 175-180.
- [28] L.L. Wei, L. Chang, Structure of coherent Mg<sub>3</sub>TiO<sub>4</sub> oxide formed between TiN and MgO, *Mater. Lett.* 213 (2018) 227-230.
- [29] B. Homayun, A. Afshar, Microstructure, mechanical properties, corrosion behavior and cytotoxicity of Mg-Zn-Al-Ca alloys as biodegradable materials, *J. Alloys. Compd.* 607 (2014) 1-10.
- [30] G.L. Song, Z.Q. Xu, The surface, microstructure and corrosion of magnesium alloy AZ31 sheet, *Electrochim. Acta.* 55 (2010) 4148-4161.
- [31] J.B. Jorcin, M.E. Orazem, N. Pébère, B. Tribollet, CPE analysis by local

- electrochemical impedance spectroscopy, *Electrochim. Acta.* 51 (2006) 1473-1479.
- [32] M.I. Jamesh, G.S. Wu, Y. Zhao, D.R. Mckenzie, M.M.M. Bilek, P.K. Chu, Electrochemical corrosion behavior of biodegradable Mg-Y-RE and Mg-Zn-Zr alloys in Ringer's solution and simulated body fluid, *Corros. Sci.* 91 (2015) 160-184.
- [33] W.H. Ma, Y.J. Liu, W. Wang, Y.Z. Zhang, Effects of electrolyte component in simulated body fluid on the corrosion behavior and mechanical integrity of magnesium, *Corros. Sci.* 98 (2015) 201-210.
- [34] P.J. Burke, Z. Bayindir, G.J. Kipouros, X-ray photoelectron spectroscopy (XPS) investigation of the surface film on magnesium powders, *Appl. Spectrosc.* 66 (2012) 510-518.
- [35] I.J.T. Jensen, A. Thøgersen, O.M. Løvvik, H. Schreuders, B. Dam, S. Diplas, X-ray photoelectron spectroscopy investigation of magnetron sputtered Mg-Ti-H thin films, *Int. J. Hydrogen Energy.* 38 (2013) 10704-10715.
- [36] L. Kuai, E. Kan, W. Cao, M. Huttula, S. Ollikkala, T. Ahopelto, A.P. Honkanen, S. Huotari, W.H. Wang, B.Y. Geng, Mesoporous  $\text{LaMnO}_{3+\delta}$  perovskite from spray - pyrolysis with superior performance for oxygen reduction reaction and Zn - air battery, *Nano. Energy.* 43 (2018) 81-90.
- [37] K. Huang, R.E. Logé, A review of dynamic recrystallization phenomena in metallic materials, *Mater. Des.* 111 (2016) 548-574.
- [38] Y.H. Sun, R.C. Wang, J. Ren, C.Q. Peng, Z.Y. Cai, Microstructure, texture, and mechanical properties of as-extruded Mg-xLi-3Al-2Zn-0.2Zr alloys (x=5, 7, 8, 9, 11 wt%), *Mater. Sci. Eng. A* 755 (2019) 201-210.
- [39] H. Esmailpour, A. Zarei-Hanzaki, N. Eftekhari, H.R. Abedi, M.R. Ghandehari Ferdowsi, Strain induced transformation, dynamic recrystallization and texture evolution during hot compression of an extruded Mg-Gd-Y-Zn-Zr alloy, *Mater. Sci. Eng. A* 778 (2020) 139021.
- [40] B.B. Dong, Z.M. Zhang, J.M. Yu, X. Che, M. Meng, J.L. Zhang, Microstructure, texture evolution and mechanical properties of multidirectional forged

- Mg-13Gd-4Y-2Zn-0.5Zr alloy under decreasing temperature, *J. Alloys. Compd.* 823 (2020) 153776.
- [41] Y.F. Wang, F. Zhang, Y.T. Wang, Y.B. Duan, K.J. Wang, W.J. Zhang, J. Hu, Effect of Zn content on the microstructure and mechanical properties of Mg-Gd-Y-Zr alloys, *Mater. Sci. Eng. A* 745 (2019) 149-158.
- [42] L. Xiao, G.Y. Yang, Y. Liu, S.F. Luo, W.Q. Jie, Microstructure evolution, mechanical properties and diffusion behaviour of Mg-6Zn-2Gd-0.5Zr alloy during homogenization, *J. Mater. Sci. Technol.* 34 (2018) 2246-2255.
- [43] G.S. Zhang, Y.Z. Meng, F.F. Yan, Z. Gao, Z.M. Yan, Z.M. Zhang, Microstructure and texture evolution of Mg-RE-Zn alloy prepared by repetitive upsetting-extrusion under different decreasing temperature degrees, *J. Alloys. Compd.* 815 (2020) 152452.
- [44] X.Y. Qian, Y. Zeng, B. Jiang, Q.R. Yang, Y.J. Wang, G.F. Quan, F.S. Pan, Grain refinement mechanism and improved mechanical properties in Mg-Sn alloy with trace Y addition, *J. Alloys. Compd.* 820 (2020) 153122.
- [45] H.F. Sun, C.J. Li, W.B. Fang, Evolution of microstructure and mechanical properties of Mg-3.0Zn-0.2Ca-0.5Y alloy by extrusion at various temperatures, *J. Mater. Process. Technol.* 229 (2016) 633-640.
- [46] J. Luo, H. Yan, R.S. Chen, E.H. Han, Effects of Gd concentration on microstructure, texture and tensile properties of Mg-Zn-Gd alloys subjected to large strain hot rolling, *Mater. Sci. Eng. A* 614 (2014) 88-95.
- [47] L. Li, Y. Wang, C.C. Zhang, T. Wang, H. Lv, Effect of Yb concentration on recrystallization, texture and tensile properties of extruded ZK60 magnesium alloys, *Mater. Sci. Eng. A* 788 (2020) 139609.
- [48] Y.Z. Du, X.G. Qiao, M.Y. Zheng, K. Wu, S.W. Xu, The microstructure, texture and mechanical properties of extruded Mg-5.3Zn-0.2Ca-0.5Ce (wt%) alloy, *Mater. Sci. Eng. A* 620 (2015) 164-171.
- [49] Q.M. Peng, B.C. Ge, H. Fu, Y. Sun, Q. Zu, J.Y. Huang, Nanoscale coherent interface strengthening of Mg alloys, *Nanoscale* 10 (2018) 18028.
- [50] Z.Y. Zhao, P.K. Bai, R.G. Guan, V. Murugadoss, H. Liu, X.J. Wang, Z.H. Guo,

- Microstructural evolution and mechanical strengthening mechanism of Mg-3Sn-1Mn-1La alloy after heat treatments, *Mater. Sci. Eng. A* 734 (2018) 200-209.
- [51] D.H. Bae, S.H. Kim, D.H. Kim, W.T. Kim, Deformation behavior of Mg-Zn-Y alloys reinforced by icosahedral quasicrystalline particles, *Acta. Mater.* 50 (2002) 2343-2356.
- [52] H.Y. Yu, H.G. Yan, J.H. Chen, B. Su, Y. Zheng, Y.J. Shen, Z.J. Ma, Effect of minor Gd addition on microstructures and mechanical properties of the high strain-rate rolled Mg-Zn-Zr alloys, *J. Alloys. Compd.* 586 (2014) 757-765.
- [53] S.Q. Yin, W.C. Duan, W.H. Liu, L. Wu, J.M. Yu, Z.L. Zhao, M. Liu, P. Wang, J.Z. Cui, Z.Q. Zhang, Influence of specific second phases on corrosion behaviors of Mg-Zn-Gd-Zr alloys, *Corros. Sci.* 166 (2020) 108419.
- [54] N. Hort, Y. Huang, D. Fechner, M. Störmer, C. Blawert, F. Witte, C. Vogt, H. Drücker, R. Willumeit, K.U. Kainer, F. Feyerabend, Magnesium alloys as implant materials – principles of property design for Mg–RE alloys, *Acta. Biomater.* 6 (2010) 1714-1725.
- [55] G.R. Argade, S.K. Panigrahi, R.S. Mishra, Effects of grain size on the corrosion resistance of wrought magnesium alloys containing neodymium, *Corros. Sci.* 58 (2012) 145-151.
- [56] Y.L. Zhou, Y.C. Li, D.M. Luo, Y.F. Ding, P. Hodgson, Microstructures, mechanical and corrosion properties and biocompatibility of as extruded Mg-Mn-Zn-Nd alloys for biomedical applications, *Mater. Sci. Eng. C* 49 (2015) 93-100.
- [57] A. Srinivasan, Y. Huang, C.L. Mendis, C. Blawert, K.U. Kainer, N. Hort, Investigation on microstructures, mechanical and corrosion properties of Mg-Gd-Zn alloys, *Mater. Sci. Eng. A* 595 (2014) 224-234.
- [58] G.L. Song, A. Atrens, Corrosion mechanisms of magnesium alloys, *Adv. Eng. Mater.* 1 (1999) 11-33.
- [59] G.L. Song, A. Atrens, Understanding magnesium corrosion: A framework for improved alloy performance, *Adv. Eng. Mater.* 5 (2003) 837-858.



- [60] F.F. Cao, K.K. Deng, K.B. Nie, J.W. Kang, H.Y. Niu, Microstructure and corrosion properties of Mg-4Zn-2Gd-0.5Ca alloy influenced by multidirectional forging, *J. Alloys. Compd.* 770 (2019) 1208-1220.
- [61] L. Yang, E. Zhang, Biocorrosion behavior of magnesium alloy in different simulated fluids for biomedical application, *Mater. Sci. Eng. C* 29 (2009) 1691-1696.
- [62] W.A. Badawy, N.H. Hilal, M. El-Rabiee, H. Nady, Electrochemical behavior of Mg and some Mg alloys in aqueous solutions of different pH, *Electrochim. Acta.* 55 (2010) 1880-1887.